Research Article | Vol. 10, No. 4 | 1 Apr 2019 | BIOMEDICAL OPTICS EXPRESS 1919
Biomedical Optics EXPRESS

Pulsed laser damage of gold nanorods in turbid media and its impact on multi-spectral photoacoustic imaging

ANDREW M. FALES,[1,*] WILLIAM C. VOGT,[1] KEITH A. WEAR,[2] ILKO K. ILEV,[1] AND T. JOSHUA PFEFER[1]

[1]*Division of Biomedical Physics, Office of Science and Engineering Laboratories, Center for Devices and Radiological Health, U.S. Food and Drug Administration, Silver Spring, MD 20993, USA*
[2]*Division of Applied Mechanics, Office of Science and Engineering Laboratories, Center for Devices and Radiological Health, U.S. Food and Drug Administration, Silver Spring, MD 20993, USA*
**andrew.fales@fda.hhs.gov*

Abstract: Innovative biophotonic modalities such as photoacoustic imaging (PAI) have the potential to provide enhanced sensitivity and molecule-specific detection when used with nanoparticles. However, high peak irradiance levels generated by pulsed lasers can lead to modification of plasmonic nanoparticles. Thus, there is an outstanding need to develop practical methods to effectively predict the onset nanoparticle photomodification as well as a need to better understand the process during PAI. To address this need, we studied pulsed laser damage of gold nanorods (GNRs) using turbid phantoms and a multi-spectral near-infrared PAI system, comparing results with spectrophotometric measurements of non-scattering samples. Transmission electron microscopy and Monte Carlo modeling were also performed to elucidate damage processes. In the phantoms, shifts in PAI-detected spectra indicative of GNR damage were initiated at exposure levels one-third of that seen in non-scattering samples, due to turbidity-induced enhancement of subsurface fluence. For exposures approaching established safety limits, damage was detected at depths of up to 12.5 mm. Typically, GNR damage occurred rapidly, over the course of a few laser pulses. This work advances the development of test methods and numerical models as tools for assessment of nanoparticle damage and its implications, and highlights the importance of considering GNR damage in development of PAI products, even for exposures well below laser safety limits.

1. Introduction

Photoacoustic (PA) imaging (PAI) is a rapidly maturing diagnostic technique that combines the high depth penetration of ultrasound with the high contrast of optical imaging. The photoacoustic process involves absorption of short light pulses by chromophores, which induce rapid heating and thermoelastic expansion, generating acoustic waves that can be detected using an ultrasound transducer placed at the tissue surface. PAI is typically performed using radiant exposures below the American National Standards Institute (ANSI) maximum permissible exposure (MPE) limits for skin, resulting in the technique generally being considered safe [1]. Many systems incorporate a tunable light source to enable multispectral sensing of chromophores, which may be quantified through spectral unmixing algorithms. PAI can be performed using endogenous chromophores, such as hemoglobin, or by delivering exogenous contrast agents with high optical absorption such as dyes and nanoparticles.

Gold nanorods are among the most widely used contrast agents for PAI, and provide the ability to perform molecular imaging of diseases such as cancer, for early detection and surgical guidance [2]. This is due to their high optical absorption and low scattering in the near-infrared (NIR) region that result from the surface plasmon resonance (SPR) effect. Gold

#348641 https://doi.org/10.1364/BOE.10.001919
Journal © 2019 Received 18 Oct 2018; revised 6 Feb 2019; accepted 8 Feb 2019; published 20 Mar 2019

Biomedical Optics EXPRESS

is also inert, biocompatible, and has a surface that can easily be modified to improve targeting and circulation. The SPR, which is highly material- and shape-dependent, is a collective oscillation of electrons on the nanoparticle surface that produces highly localized electromagnetic field enhancement when excited with the appropriate wavelength of light. Experimental techniques allow for precise tuning of the length and width of gold nanorods, and therefore, the position of the SPR within the NIR region.

Gold nanorod-based PAI contrast agents have been used in a variety of preclinical applications. Specific targeting to cancer biomarkers has allowed for PA detection of tumors in living mice [3–5]. Gold nanorods in circulation have also been used for cardiovascular imaging and circulating tumor cell detection [6,7]. Theranostic applications, combining diagnostic PAI with a therapeutic modality such as photothermal therapy, show great promise for cancer detection and treatment [8]. Multispectral PAI can be used to separate the gold nanorod spectral signal from the endogenous background, thus improving sensitivity [9].

While PAI employs levels of laser exposure that are generally recognized as safe, previous studies have shown that radiant exposures below the ANSI limit can reshape nanorods [10–13]. In most cases, there has been no objective and quantitative evaluation to determine the damage threshold of gold nanorods. Rather, the first observed change in the absorbance spectrum or photoacoustic signal intensity is arbitrarily defined as the damage threshold. In this work, we implement the use of a dose-response curve based on the SPR peak of the nanorod sample to quantitatively define the damage threshold, similar to our previously developed approach for gold nanospheres [14]. Although it is currently unclear whether nanorod melting and reshaping will cause any harmful biological effects, this will severely impact the effectiveness of gold nanorod PAI contrast agents as reshaping will move the SPR away from the laser excitation wavelength.

Another aspect of pulsed laser-nanoparticle interaction that has not been rigorously studied is the effect of a turbid medium on the damage thresholds. Multiple scattering in tissue can produce maximum fluence levels beneath the tissue surface that greatly exceed the surface radiant exposure [10]. Not only would this increased fluence effectively lower damage thresholds based on radiant exposure for superficial targets, but the thresholds would be variable depending on the tissue optical properties, which are known to have variation with tissue composition [15]. This could be an important factor in determining the optimal radiant exposure to maintain effective PAI contrast in specific tissues.

A previous report by Didychuk *et al.* used NIR reflectance imaging combined with Monte Carlo simulations to estimate the depth and threshold for nanorod conversion within a tissue-mimicking gel [10]. While these results are of interest, the study design and phantom used were aimed at evaluating the use of GNRs for photothermal therapy. In the case of PAI, instead of a uniform distribution of GNRs within the phantom, a more relevant design would have a GNR inclusion within a background medium. This report did not include any PAI experiments, or spectral measurements, and the phantoms were not reusable, making them non-ideal for use in a test method.

Cavigli *et al.* studied the effect of nanorod size on their conversion in a thin chitosan film [13]. This study was focused on determining the physical mechanisms that influence nanorod stability in photoacoustic applications. Again, the phantom contained a uniform distribution of nanorods that was irradiated on the surface and is not reusable. PA measurements were performed using a needle hydrophone at a single excitation wavelength, which cannot address the effect of nanorod conversion on multispectral PA imaging. The optical properties of the films were not characterized, and their thickness (~50 μm) prohibited investigation of conversion depth.

While both of these previous works provided insight about nanorod reshaping in turbid media and during photoacoustic applications, respectively, there have been no reports that investigate both the stability of nanorods in turbid media and the impact of their reshaping on PAI together. The primary goal of this work is to understand the practical implications of

Biomedical Optics EXPRESS

GNR damage processes on PAI for medical applications. In this report, we first quantitatively evaluate the pulsed laser-induced damage thresholds of 800 nm resonant gold nanorods in solution using a spectrophotometric-based test method. Fluence effects on nanorod damage due to scattering are investigated using a turbid medium-filled phantom (1% Intralipid) with a biologically relevant reduced scattering coefficient (~10 cm^{-1} at 800 nm). Nanorod damage and the resulting effect on PA signal intensity are monitored within this turbid phantom. Monte Carlo simulations are used to estimate the depth- and wavelength- dependent fluence within the phantom. Spectrophotometric data is compared to PAI results to determine the most appropriate threshold definition from the dose-response curve to predict a significant degradation in performance of a nanorod contrast agent.

2. Methods

2.1 Cuvette-based particle damage exposures

We first developed a benchtop spectrophotometric test method for quantifying nanoparticle damage as a function of laser radiant exposure. A third harmonic (355 nm), Q-switched Nd:YAG laser (Surelite III-10; Continuum, San Jose, CA) was used to pump an optical parametric oscillator (OPO) (Surelite OPO; Continuum) to provide 3-5 ns pulses at the desired wavelength. Pulse energy was controlled with a Glan-Taylor prism (GL10, Thorlabs; Newton, NJ) and measured with a pyroelectric energy sensor (PE10-SH-V2; Ophir, Israel). The laser emission was coupled into a multimode fiber (F-MTC, Newport; Irvine, CA) with a fiber-coupling stage (F-91-C1, Newport; Irvine, CA) and delivered to the sample using a cuvette holder (CUV-ALL-UV, Ocean Optics; Largo, FL) with a 3.0 mm aperture collimating lens. For each exposure, the gold nanorod (GRGN800, NanoComposix; San Diego, CA) solution (1 OD, 3 mL) was placed into a disposable cuvette (Type 1FLP, FireflySci; Brooklyn, NY) with a magnetic stir bar (Z363545, Sigma-Aldrich; St. Louis, MO) and inserted into the cuvette holder. Each sample was irradiated for 5 minutes at the specified radiant exposure (energy measured through a 3.5 mm limiting aperture, per ANSI Z136.1) while stirring to ensure that the total sample volume was homogenously exposed, performed in triplicate. These samples were analyzed by spectrophotometry in a similar manner to our previous report with gold nanospheres [14]. Absorbance spectra were collected over 400–1300 nm using a dual-beam UV/VIS/NIR spectrophotometer (Lambda 1050, PerkinElmer; Waltham, MA) in the 10 mm path length cuvettes used for exposure. Transmission electron microscopy (TEM) samples were prepared by drop-casting 2 μL of nanoparticle solution onto a Formvar/carbon-coated copper grid and allowing it to dry. TEM micrographs were recorded on a JEM-1400 (JEOL Inc., Peabody, MA) operating at an accelerating voltage of 80 kV.

2.2 PAI system and image processing

Photoacoustic imaging and scattering phantom exposures were performed using a custom PAI system described previously [16]. The system consists of an OPO (Phocus Mobile; Opotek, Inc., Carlsbad, CA) and 128-channel research-grade ultrasound system (Vantage 128; Verasonics, Inc., Seattle, WA). The OPO was upgraded to enable fast wavelength tuning at the 10 Hz repetition rate, allowing for fast multispectral PAI. Multispectral imaging scans were performed using 100 wavelengths (700 to 898 nm in 2 nm steps). The radiant exposure at 800 nm was measured using a 3.5 mm aperture and energy meter (J-50MB-HE; Coherent, Santa Clara, CA). Laser light was directed to the sample using a 6-mm diameter, 0.22 NA fiber bundle. A 128-element linear-array transducer (L11-4v; Verasonics) with 8.0 MHz center frequency, 8.7 MHz –20 dB bandwidth, and 38.1 mm aperture length was used to detect photoacoustic signals. The transducer was covered with aluminum foil to reduce photoacoustic signal generation from reflected light impinging on the transducer surface. Pulse-to-pulse energy variation was corrected using an internal energy meter. Real-time

Biomedical Optics EXPRESS

display, image acquisition, and reconstruction are performed using Matlab (The Mathworks, Inc., Natick, MA).

'Spectral coloring' is a well-known artifact in multispectral PAI, where the background tissue optical properties filter the local fluence received by an absorptive target and corrupt measurements of the target's absorption spectrum [17]. A depth- and wavelength-dependent fluence correction was applied to collected images using a 1D fluence model based on Monte Carlo simulations performed using MCML [18]. Simulations were performed using the optical properties of 1% Intralipid (I141, Sigma-Aldrich) in the spectral range of 700-900 nm, with absorption coefficient, $\mu_a(\lambda)$, from measurement of the absorption spectrum of water, and scattering coefficient, $\mu_s(\lambda)$, and anisotropy, $g(\lambda)$, approximated according to van Staveren et al. [19] with one million photons and a 0.01 cm grid spacing. Beam geometry was 1.2 cm diameter Gaussian at normal incidence, and the central portion of the beam was used for the fluence correction. PAI spectra were smoothed using a first-order Savitzky-Golay filter with a window length of 21. Data analysis was performed using NumPy, SciPy, and Matplotlib within the Anaconda Python distribution [20–22].

2.3 Nanorod exposures in turbid phantom

2.3.1 Effect of depth and surface radiant exposure

A liquid phantom was prepared using a 7 × 7 × 5 cm acrylic chamber containing 0.5 mm inner diameter PTFE tubes (STT-24, Component Supply Company, Inc., Sparta, TN) suspended at depths of 4, 5, 6, 8, 10, 12.5, and 15 mm. The chamber was filled with a 1% dilution of Intralipid in deionized (DI) water with a reduced scattering coefficient (μ_s') of ~10 cm^{-1} at 800 nm, which is similar to that of breast tissue [23]. For imaging, a 2-cm thick standoff pad (Aquaflex; Parker Laboratories, Inc., Fairfield, NJ) was placed on top of the phantom to allow centering of the laser spot beneath the transducer, ensuring maximal optical exposure in the image plane (see Fig. 1). A pre-exposure spectral scan was collected at low energy (2-6 mJ/cm^2 depending on depth) to obtain the undamaged nanorod spectrum. For exposures, one tube was filled with 1 OD nanorod solution at a time and centered under the laser spot (~1.25 cm), which was adjusted to normal incidence at the phantom surface without a standoff pad. Exposure of the sample was performed at the nanorod nominal resonance peak (800 nm, 1000 pulses), with a radiant exposure of 10.0 ± 0.9 mJ/cm^2, 20 ± 2 mJ/cm^2, or 30 ± 1 mJ/cm^2 (measured through a 3.5 mm aperture placed at the same distance to the fiber bundle as the sample surface). These values were chosen as 20 mJ/cm^2 is often reported in the literature for PAI, and 30 mJ/cm^2 is near the ANSI MPE at 800 nm (31.7 mJ/cm^2). Another low-energy scan was performed after exposure to observe any changes in the PAI spectrum. The tube was then flushed with DI water to remove any residual particle solution.

Biomedical Optics EXPRESS

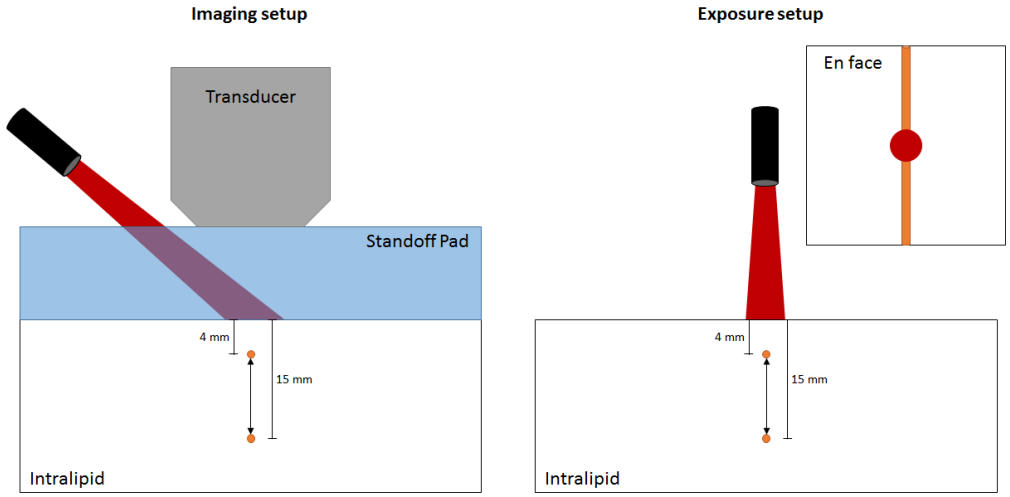

Fig. 1. Schematic of the photoacoustic imaging (left) and nanorod exposure (right) experimental setups (not to scale).

2.3.2. Spatial extent of nanorod damage and effect on image quality

To demonstrate the impact that nanorod damage can have on performance as a contrast agent we performed irradiation of a 5-mm deep tube with a radiant exposure of ~20 mJ/cm^2 at 800 nm, near the center of the phantom. Multispectral PAI scans were performed with imaging plane perpendicular to the tube axis in 3-mm steps.

2.3.3. Temporal stability of nanorods during PAI

The temporal stability of nanorods during PAI was studied by monitoring the PA signal from the nanorod-filled tubes at ~20 mJ/cm^2 radiant exposure. In this case, the laser energy was delivered at an angle (as in the imaging configuration shown in Fig. 1) in order to irradiate and image the same area simultaneously. Each sample was exposed to 1000 pulses at 800 nm excitation, followed by a PA spectral scan.

2.3.4. Nanorod damage thresholds *in situ*

The lowest possible radiant exposure for inducing nanorod damage was determined using the 4-mm deep tube as a worst-case scenario. Exposures of 1000 pulses were performed at radiant exposure levels from 1 to 5 mJ/cm^2. After each exposure, a PA spectral scan was collected, and the tube was replenished with fresh nanorod solution.

3. Results and discussion

3.1 Cuvette-based particle damage exposures

The TEM images (Fig. 2) show nanorod reshaping from rod to ϕ-shaped occurs at radiant exposures as low as 15 mJ/cm^2, with a significant reduction in rod-shaped particles achieved at 20 mJ/cm^2. The ϕ-shaped particles observed in Fig. 2 do not occur in the stock solution and are well-known as a product of nanorod melting [24–26]. These findings are significant, as the per-pulse ANSI MPE for skin at this wavelength is 31.7 mJ/cm^2, indicating poor stability of nanorods even below the ANSI limit.

Biomedical Optics EXPRESS

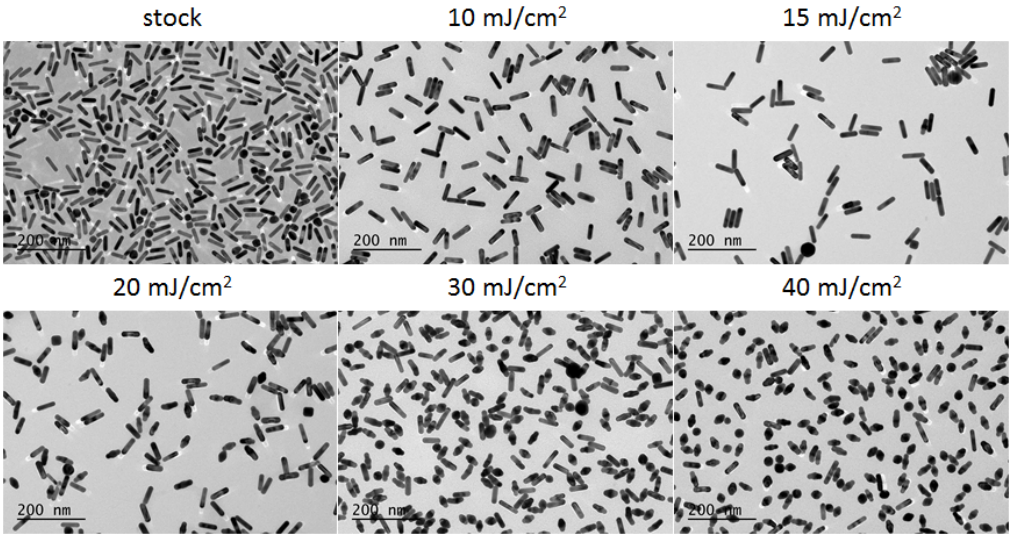

Fig. 2. TEM micrographs of the 800-nm resonant nanorods at the indicated radiant exposures. All scale bars are 200 nm.

The optical properties of these samples were evaluated by spectrophotometry. As seen in Fig. 3(a), a significant shift in the spectrum of the nanorods is observed when the radiant exposure is increased to 15 mJ/cm^2. Further increasing the radiant exposure causes a depletion in absorbance near the original resonance peak, resulting in a splitting of the longitudinal band. This effect can be attributed to the distribution of nanorod sizes in the sample [27,28]. Nanorods with slightly higher or lower aspect ratios do not absorb as much energy with on-resonance excitation, causing only the nanorods with high absorption at 800 nm to undergo reshaping. This is also evidenced in the TEM images, where even at 40 mJ/cm^2 radiant exposure there are still intact rods. The remaining rods appear mostly at lower aspect ratios compared to stock, with a few higher aspect ratio rods observed.

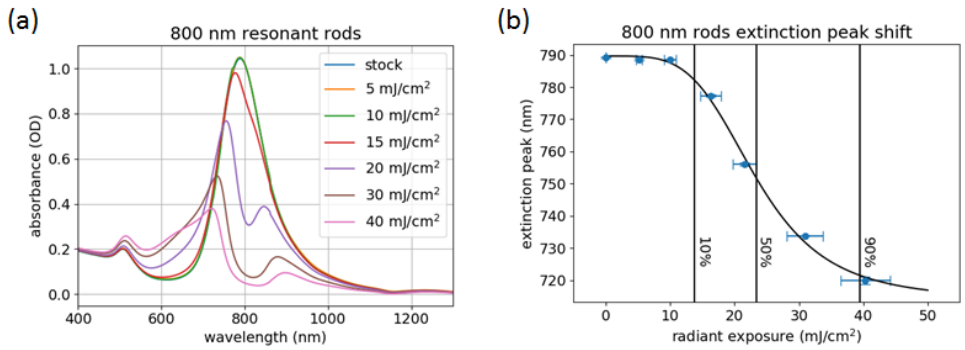

Fig. 3. Absorbance spectra of the 800-nm resonant nanorods at different radiant exposures (a), and plasmon peak position as a function of radiant exposure (b). The stock, 5 mJ/cm^2, and 10 mJ/cm^2 spectra in (a) are overlapped, indicating that nanorod shape is stable at these exposure levels. The 10, 50 and 90% lines in (b) correspond to 13.8 ± 0.7, 23 ± 1, and 40 ± 2 mJ/cm^2, respectively.

To quantitively evaluate the nanorod damage process, the plasmon peak position was plotted as a function of radiant exposure (Fig. 3(b)). These data were fit with a four-parameter sigmoidal dose-response curve as a way to quantify the extent of nanorod reshaping at a specific radiant exposure. Depending on the intended application, different threshold levels

Biomedical Optics EXPRESS

(10%, 50%, 90%, etc.) could be used. In the case of contrast agents, a low value, such as 10%, would be appropriate to ensure limited changes in signal due to particle damage. A report by Chen *et al.* studied the effect of different surface coatings on GNR stability after laser irradiation [12]. No quantitative evaluation of the damage threshold was performed; however, a change in the extinction spectra of PEG-coated GNRs was observed at 12 mJ/cm^2, which is similar to what we have observed (Fig. 3). While this cuvette-based test method allows for reproducible and quantitative evaluation of nanorod damage, it does not account for fluence effects that can occur when imaging *in vivo*. Light scattering within biological tissues can produce sub-surface fluences much higher than the incident radiant exposure. For investigation of these effects, we have prepared a liquid phantom with biologically-relevant scattering properties.

3.2 Nanorod exposures in turbid phantom

3.2.1 Effect of depth and surface radiant exposure

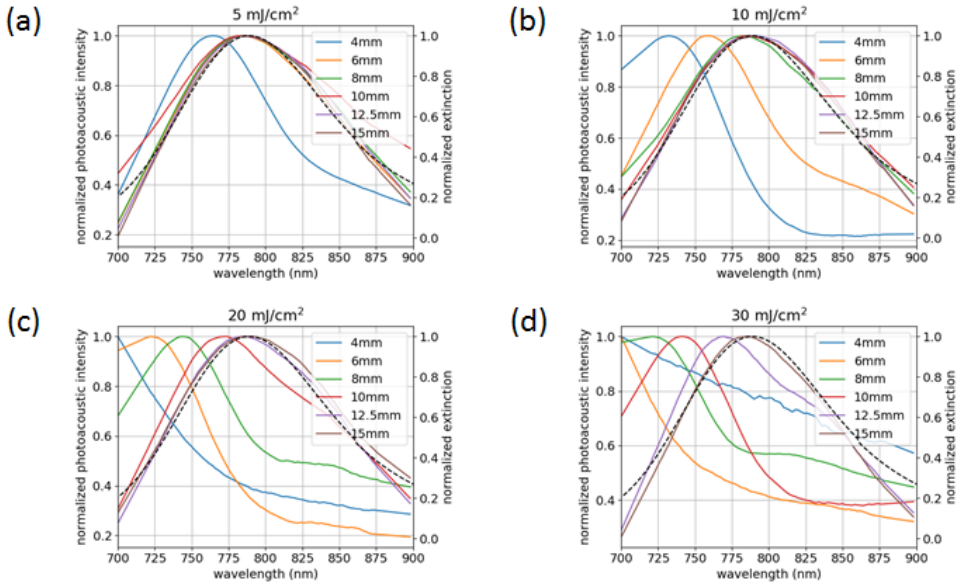

Fig. 4. (a) Photoacoustic spectra of the nanorod samples after exposure at 5.0 ± 0.5 mJ/cm^2 (left axis, colored lines) compared to spectrophotometric data from the stock sample (right axis, dashed black line). (b) Exposure at 10.0 ± 0.9 mJ/cm^2. (c) Exposure at 20 ± 2 mJ/cm^2. (d) Exposure at 30 ± 1 mJ/cm^2.

Figure 4 shows the measured PA spectra of the nanorod samples after irradiation at different radiant exposures. All spectra are normalized to their maximum value. A significant spectral shift is observed at the 4-mm depth for all radiant exposures. At 10 mJ/cm^2, spectral changes occur up to 6-mm depth; at 20 mJ/cm^2, up to 10-mm depth; and at 30 mJ/cm^2, up to 12.5 mm depth. In the case of the 4-mm tube at 30 mJ/cm^2 (Fig. 4(d)), the peak has shifted out of the collectable range, resulting in a quasi-linear spectral response. The PA spectra show similar blue-shifting behavior to the spectra from the cuvette damage experiment that were measured by spectrophotometry (Fig. 3). The dip and secondary peak observed by spectrophotometry do not show up as prominently in the PA spectra. This is due to multiple factors, including the limited spectral range, the spectral bandwidth of the laser (~4 nm FWHM at 800 nm and increases with wavelength), and sensitivity of the ultrasound system. To further investigate the effects of depth on nanorod damage, we can use Monte Carlo simulations to estimate the fluence incident upon each tube during exposure (Fig. 5).

Biomedical Optics EXPRESS

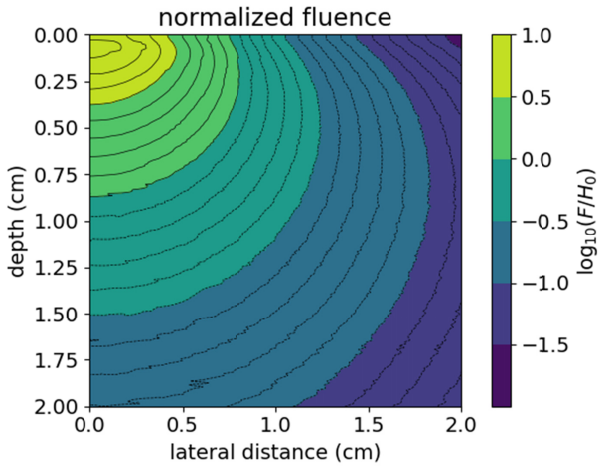

Fig. 5. Calculated fluence (F) map using the optical properties of 1% Intralipid at 800 nm with a normal incidence Gaussian beam (1.25 cm diameter), normalized to the incident radiant exposure (H_0). Values greater than zero indicate fluence exceeding the incident radiant exposure.

Since the tubes are centered in the beam during exposure, the fluence values vs. depth were taken at the center of the beam (r = 0). The maximum fluence reached is 7 × the incident radiant exposure at a depth of 0.7 mm. The fluence exceeds the radiant exposure up to a depth of 8.4 mm. Fluence values at each of the six depths were calculated for the four radiant exposures used. These results have been compiled into Table 1. The estimated fluence values for each depth are in good agreement with the matched cuvette-PAI data. By using the dose-response curve in Fig. 3(b), we can predict the plasmon peak shift of the samples at different depths with a given radiant exposure. These data suggest that the 10% threshold (13.8 ± 0.7 mJ/cm^2) for damage as determined by spectrophotometry would be most appropriate to avoid altering the nanorod PA spectrum, and that fluence effects must be considered when imaging in turbid media. At the maximum radiant exposure used (30 mJ/cm^2), the Monte Carlo simulation gives a fluence above 13.8 mJ/cm^2 up to 12.8 mm depth, which is in good agreement with our PA spectral data (Fig. 4(d)).

These results indicate that the combination of experimental nanorod damage data in cuvettes and Monte Carlo simulation may be an effective method to predict the depths at which damage is likely to occur in a medium with known optical properties. It might also be possible to predict the spectral shifts expected for a given radiant exposure and depth, but spectral coloring effects and spectral data processing used to correct these effects may present challenges in directly predicting PA spectra. Although the Monte Carlo code used in this study is not capable of simulating realistic, non-circular beam geometries commonly used in PAI, the large circular beam used in this study can be considered as a worst-case scenario since it will generate the greatest subsurface fluence compared to other beam geometries.

Biomedical Optics EXPRESS

Table 1. Estimated fluence (mJ/cm^2) at each tube depth and radiant exposure using the Monte Carlo simulation data at 800 nm excitation. (*) indicates fluence above the 10% threshold from the dose-response curve in Fig. 3(b) where spectral changes are expected to occur.

Depth / Radiant Exposure	5.0 ± 0.5 mJ/cm^2	10.0 ± 0.9 mJ/cm^2	20 ± 2 mJ/cm^2	30 ± 1 mJ/cm^2
4 mm	15 ± 1*	30 ± 3*	60 ± 6*	89 ± 4*
6 mm	8.9 ± 0.8	18 ± 2*	36 ± 3*	53 ± 2*
8 mm	5.8 ± 0.5	12 ± 1	23 ± 2*	35 ± 2*
10 mm	3.9 ± 0.4	7.8 ± 0.7	16 ± 1*	23 ± 1*
12.5 mm	2.4 ± 0.2	4.9 ± 0.4	9.7 ± 0.9	14.6 ± 0.7*
15 mm	1.6 ± 0.1	3.2 ± 0.3	6.5 ± 0.6	9.7 ± 0.5

To the best of our knowledge, there has only been one previous report (Didychuk *et al.*) investigating the pulsed-laser-induced reshaping of GNRs in turbid phantoms [10]. In their study, GNRs were embedded in agarose gel phantoms that were then exposed to ns-pulses and assessed by NIR imaging. The depth and radius of conversion were determined by taking the transmitted light intensity profile along the longitudinal axis or diameter, respectively, using the FWHM (50% of the maximum intensity) as the determined value. Monte Carlo simulations were then used to estimate the fluence at each of the determined depths to deduce a threshold value of 34.2 ± 8.5 mJ/cm^2. While somewhat higher than our 50% threshold of 23 ± 1 mJ/cm^2, this may be due to the fact that smaller nanorods (32 ± 4 nm length, 9 ± 1 nm width) were used compared to our study (58 ± 4 nm length, 16 ± 1 nm width), as well as a smaller beam size (10-mm Gaussian through an 8-mm aperture) that would reduce fluence effects. It has been shown that nanorod damage thresholds decrease as particle size increases [13]. Another factor is that NIR imaging may not be as sensitive as spectrophotometry to changes in GNR absorption, which could cause an underestimation of the conversion depth and an overestimation of the damage threshold. At 30 mJ/cm^2 radiant exposure, Didychuk found a depth of conversion up to 7.6 mm, compared to 12.5 mm in our study. The main factor in this difference is the absorption coefficient of the phantoms used. The nanorod-embedded gels had a μ_a of 0.1 cm^{-1}, whereas our Intralipid phantom had a μ_a of 0.01 cm^{-1}, both at 800 nm. We repeated the Monte Carlo simulation using the optical properties reported by Didychuk to estimate the depth of conversion using our experimentally determined threshold of 13.8 mJ/cm^2, finding the fluence to exceed this value up to a depth of 8.6 mm. This is higher than the 7.6 mm reported by Didychuk and may be explained by the smaller nanorods used in their study having a higher damage threshold than the ones we have used. While this phantom approach provided insightful results, it is not as conducive to performance testing for PAI as a phantom with discrete channels that are reuseable/refillable.

A study by Cavigli *et al.* used GNR-embedded chitosan films to evaluate the effect of nanorod size on their reshaping threshold [13]. The PA signal response after laser irradiation was used to monitor resultant changes in the GNRs. The first statistically significant decrease in PA intensity was defined as the threshold. Depending on the size of GNR used, the threshold varied from 6.5 ± 1 mJ/cm^2 to 2 ± 0.5 mJ/cm^2. It is difficult to compare these values to our results as the optical properties of the chitosan film are unknown.

Biomedical Optics EXPRESS

3.2.2 Spatial extent of nanorod damage and effect on image quality

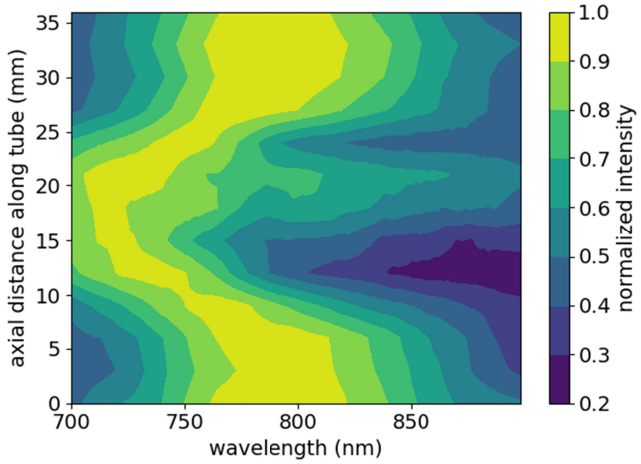

Fig. 6. Contour plot of photoacoustic spectra collected from a 5-mm deep tube while scanning along its length in 3-mm steps.

A contour plot of the extracted spectra from the tube region is shown in Fig. 6. A clear region of significantly altered PA spectra is observed at distances of about 10-22 mm, when the imaging plane crosses through the damage zone. The original plasmon peak of the stock nanorods occurring near 800 nm is increasingly blue-shifted while moving towards the center of the exposure area. The central portion of the damage zone is similar in size to the beam size used for exposure (~1.25 cm). From our Monte Carlo simulation, at 5-mm depth, the fluence exceeds the 13.8 mJ/cm^2 damage threshold up to 7 mm from the center of the beam, suggesting a total damage zone of 14 mm. The experimental data show significant spectral changes starting at 9 mm and extending up to 24 mm, resulting in a 13-mm zone of damage. With finer sampling along the tube length, the experimental and simulated damage zones could show better agreement. The effect of these spectral changes on PAI quality were assessed by measuring the signal-to-background ratio (SBR) and contrast-to-noise ratio (CNR) of the imaged tube at 800 nm in an undamaged and damaged region of the tube (Fig. 7).

Biomedical Optics EXPRESS

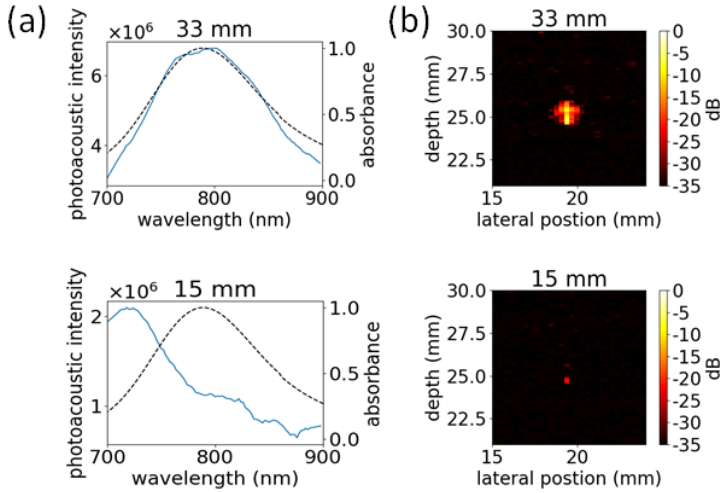

Fig. 7. (a) Photoacoustic spectra collected from an undamaged (33 mm) and damaged (15 mm) location along the tube length. (b) Photoacoustic images of the tube at an undamaged (33 mm) and damaged (15 mm) location, collected at 800 nm.

As shown in Fig. 8, the blue-shift and reduction in signal of the particles after damage results in much lower contrast from the target. To quantitatively evaluate this difference, SBR and CNR were calculated according to: $\boldsymbol{SBR} = \frac{\bar{x}_s}{\bar{x}_b}$; $\boldsymbol{CNR} = \frac{|\bar{x}_s - \bar{x}_b|}{\sigma_b}$, where $\bar{x}_s$ is the average signal from the target, $\bar{x}_b$ is the average signal from the background, and σ_b is the standard deviation of the background. The values were calculated from ROIs, thresholded to 50% of the maximum value, drawn over and adjacent to the tube. These results have been tabulated in Table 2.

Table 2. Calculated SBR and CNR from the images in Fig. 8(b).

Lateral Position	33 mm	15 mm
SBR	29.9 ± 0.5	4.5 ± 0.4
CNR	60 ± 1	14.0 ± 0.9

There is >6 × reduction in the SBR and >4 × reduction in CNR for the damaged vs. undamaged area. This indicates that reshaping of GNR PAI contrast agents can significantly impact signal intensity, and thus detectability, especially in shallow targets.

Biomedical Optics EXPRESS

3.2.3 Temporal stability of nanorods during PAI

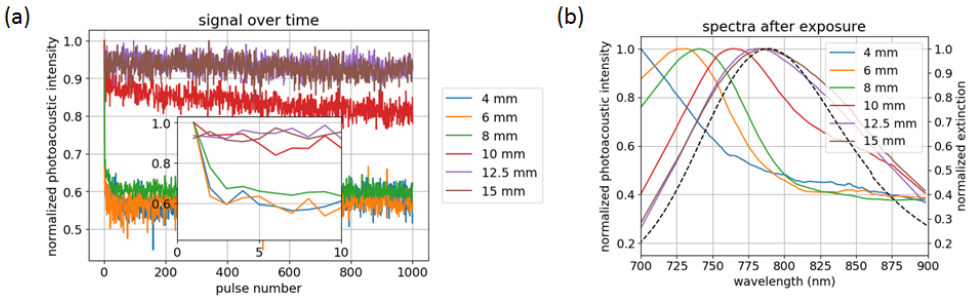

Fig. 8. (a) Photoacoustic signal from the different tubes with 800 nm irradiation at ~20 mJ/cm^2 radiant exposure over 1000 pulses. Inset: expanded view of photoacoustic signal over the first 10 pulses. (b) Resultant photoacoustic spectra after irradiation.

The PA intensity obtained with 800-nm exposure from the tubes at different depths and the PA spectra after irradiation are shown in Fig. 8. The shallowest tubes, at 4, 6, and 8 mm depths, show an almost instantaneous decrease in PA signal, while the 10-mm tube has a gradual decay in signal over the course of the exposure (Fig. 8(a)). At 12.5 and 15 mm depths, the signal has little variation over the 1000 pulses and there is no discernable change in the PA spectrum after exposure (Fig. 8(b)). The observation of continued signal degradation over time is a result of progressively damaging the nanorods in the irradiated volume. At higher radiant exposures, the initial sharp decrease in signal is likely due to damaging particles located in the center of the beam, while the slower decay in signal after the first pulse can be attributed to particles at the periphery of the beam undergoing reshaping, where the laser energy is lower.

Data on the time course of GNR damage in the literature are limited. Didychuk noted nanorod conversion occurring after a single pulse, with the effect continuing up to about 100 pulses, where the depth and radius of conversion plateaued [10]. We also observed a rapid initial change that then plateaued for shallow tubes, though this occurred in less than 10 pulses. Differences in the optical properties and geometry of the phantom, the medium surrounding the nanorods, and the method used to detect GNR changes make quantitative comparison to our work problematic. In a study also using PA intensity to detect GNR changes, Cagivli found that exposures much higher than the damage threshold produced a significant reduction in PA signal within the first few pulses, while exposures slightly above the threshold showed a more gradual change in signal [13]. This is similar to the response we observed in Fig. 8, where the shallow tubes show an instantaneous drop in PA signal but deeper tubes gradually decrease in signal over the course of the exposure.

Biomedical Optics EXPRESS

3.2.4 Nanorod damage thresholds *in situ*

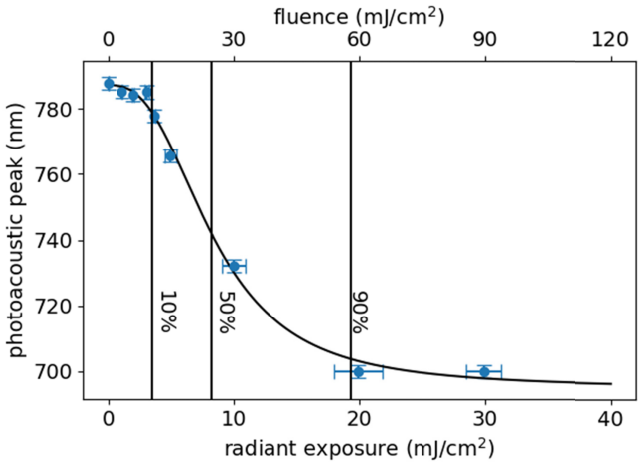

Fig. 9. Photoacoustic peak position acquired from the 4-mm deep tube after irradiation at the specified radiant exposures. The 10, 50, and 90% lines correspond to 3.7 ± 0.2, 8.3 ± 0.5, and 19 ± 1 mJ/cm^2, respectively.

The PA spectral peak positions obtained from the 4-mm deep tube at increasing radiant exposures are shown in Fig. 9. We previously observed a spectral shift for the 4-mm tube at 5 mJ/cm^2 (Fig. 4) and decided to investigate the lower bound at which nanorod damage can occur by using radiant exposures in the range of 1 – 4 mJ/cm^2. As seen in Fig. 9, there is no discernable change in the PA peak up to 3 mJ/cm^2. At ~4 mJ/cm^2, a slight blue-shift of the peak is noticeable; however, the intensity at 800 nm is still greater than 90% of the maximum (data not shown). Only at 5 mJ/cm^2 do we see a substantial drop in PA signal at the excitation wavelength. To quantitatively assess the effect of radiant exposure on PA peak position, the data were fit with a dose-response curve in a similar manner to Fig. 3(b). The various dose-response levels from the fitting are shown in Table 3.

Table 3. Radiant exposure levels and estimated fluence obtained from the dose-response curve in Fig. 9. These values are compared to those obtained from the cuvette-based spectrophotometric method (Fig. 3(b)).

Dose-response	Radiant Exposure (mJ/cm^2)	Fluence (mJ/cm^2)	Cuvette Data (mJ/cm^2)
10%	3.7 ± 0.2	11.1 ± 0.7	13.8 ± 0.7
50%	8.3 ± 0.5	25 ± 2	23 ± 1
90%	19 ± 1	57 ± 4	40 ± 2

In order to compare these data to the previous cuvette spectrophotometer data, results from the Monte Carlo simulation were used to estimate the fluence incident on the tube at the given radiant exposures. The fluence-corrected 10% and 50% values show good agreement with those obtained from the cuvette data. The discrepancy at 90% is likely due to the sparse sampling above 5 mJ/cm^2, and the limited spectral range of the PAI system, which could be masking a sharper change in peak wavelength above 10 mJ/cm^2. This suggests that using the 50% value, where sensitivity is the highest, with a built-in safety factor (*e.g.* 1/10) may be the most reliable method for defining a maximum exposure level with nanorod contrast agents.

3.3 Implications for PAI performance testing and tissue imaging

While numerous reports about GNR reshaping under pulsed laser exposure can be found in the literature, this fact is often overlooked when GNRs are applied as PA contrast agents [5,9,29–32]. There is also a lack of phantom-based test methods suitable for performance

Biomedical Optics EXPRESS

testing of GNR contrast agents. The only prior study of GNR in turbid phantoms used agarose gels embedded with a uniform distribution of GNR [10]. Such phantoms are not reusable and are also not suitable for PAI performance testing. Cavigli also used a uniform distribution of GNR in their chitosan film phantom, which has similar drawbacks [13]. In contrast, the liquid phantoms used in this study allow for rapid tuning of the optical properties of the medium, and GNR-filled tubes as targets make the phantom reusable. The data generated from this phantom indicate that use of GNR contrast agents in PAI at shallow depths poses a potential for performance degradation at radiant exposures below current safety limits.

There continue to be uncertainties regarding the fate of nanoparticles when applied *in vivo*. Cell studies have shown that different cell lines, active vs. passive targeting, and incubation times can all influence the rate of nanoparticle internalization. Particles bound to a cell's surface can be detected prior to internalization and clustering depending on the time-point [33,34]. Clustering of particles will alter their plasmon resonance and may impact their PA response. However, *in vivo*, extravasation of nanoparticles in the tumor region does not necessarily result in the internalization of the particles, and previous studies have shown strong photoacoustic signal detectable in tumors after intravenous injection of GNRs [5,35–37]. Our study is meant to highlight the importance of characterizing the photostability of such contrast agents, and provide test methodologies that can be applied to gold nanorods of different sizes and aspect ratios (which affect their photostability). These methods may also be valid for characterization of other shapes of gold nanoparticles or particles made of different materials, as well as other biomedical techniques combining gold nanoparticles and pulsed lasers, such as optoporation, plasmonic nanobubble generation, and neural and cardiac stimulation [38–43].

4. Conclusion

Gold nanorod laser damage processes and their impact on spectral PAI measurements were experimentally evaluated using a multi-channel turbid phantom approach. Additionally, damage thresholds were determined and compared to results obtained with our previously developed spectrophotometric test method. Exposure of nanorod targets in a turbid phantom to pulsed laser irradiation at radiant exposures below the ANSI MPE for skin showed significant changes in PA spectra for targets as deep as 12.5 mm. Fluence predictions from Monte Carlo simulations enabled comparison of damaged GNR PAI spectra from turbid phantoms to spectra measured in cuvettes by spectrophotometry. Image quality metrics were used to show the reduction in performance of GNR contrast in PAI resulting from particle damage. Temporal stability of the nanorod signal during PAI showed rapid degradation, within the first couple of pulses, can occur depending on target depth and fluence experienced. In conclusion, we have demonstrated that nanorod damage can occur at 'tissue-safe' radiant exposures in turbid media, we were able to correlate *in situ* damaged GNR PAI spectra to a robust benchtop method using Monte Carlo simulation, and these results indicate that nanoparticle damage is important to consider for preclinical and clinical applications of nanoparticle-enhanced PAI.

Funding

CDRH/FDA Nanotechnology Research Program; FDA Collaborative Opportunities for Research Excellence in Science Program (CORES); FDA Medical Countermeasures initiative (MCM282); ORISE Research Participation Program at the Center for Devices and Radiological Health

Acknowledgments

Portions of this work were presented at the OSA Frontiers in Optics / Laser Science Conference in 2018, paper FM3F.4. The authors would like to acknowledge constructive input from Dr. Pejhman Ghassemi (FDA) on *in vitro* approaches for evaluating spectral

Biomedical Optics EXPRESS

changes in nanoparticle absorption. The authors acknowledge the FDA Advanced Characterization Facility for use of their TEM.

Disclosures

The authors declare that there are no conflicts of interest related to this article. The mention of commercial products, their sources, or their use in connection with material reported herein is not to be construed as either an actual or implied endorsement of such products by the U.S. Department of Health and Human Services.

References

1. American National Standards Institute, American National Standard for the Safe Use of Lasers, Orlando, FL: ANSI; Z136.1; 2014.
2. W. Li and X. Chen, "Gold nanoparticles for photoacoustic imaging," Nanomedicine (Lond.) **10**(2), 299–320 (2015).
3. P.-C. Li, C.-R. C. Wang, D.-B. Shieh, C.-W. Wei, C.-K. Liao, C. Poe, S. Jhan, A.-A. Ding, and Y.-N. Wu, "In vivo photoacoustic molecular imaging with simultaneous multiple selective targeting using antibody-conjugated gold nanorods," Opt. Express **16**(23), 18605–18615 (2008).
4. H. Cui and X. Yang, "In vivo imaging and treatment of solid tumor using integrated photoacoustic imaging and high intensity focused ultrasound system," Med. Phys. **37**(9), 4777–4781 (2010).
5. J. V. Jokerst, A. J. Cole, D. Van de Sompel, and S. S. Gambhir, "Gold nanorods for ovarian cancer detection with photoacoustic imaging and resection guidance via Raman imaging in living mice," ACS Nano **6**(11), 10366–10377 (2012).
6. V. P. Zharov, E. I. Galanzha, E. V. Shashkov, N. G. Khlebtsov, and V. V. Tuchin, "In vivo photoacoustic flow cytometry for monitoring of circulating single cancer cells and contrast agents," Opt. Lett. **31**(24), 3623–3625 (2006).
7. A. Taruttis, E. Herzog, D. Razansky, and V. Ntziachristos, "Real-time imaging of cardiovascular dynamics and circulating gold nanorods with multispectral optoacoustic tomography," Opt. Express **18**(19), 19592–19602 (2010).
8. Y. Du, Q. Jiang, N. Beziere, L. Song, Q. Zhang, D. Peng, C. Chi, X. Yang, H. Guo, G. Diot, V. Ntziachristos, B. Ding, and J. Tian, "DNA-Nanostructure-Gold-Nanorod Hybrids for Enhanced In Vivo Optoacoustic Imaging and Photothermal Therapy," Adv. Mater. **28**(45), 10000–10007 (2016).
9. E. Herzog, A. Taruttis, N. Beziere, A. A. Lutich, D. Razansky, and V. Ntziachristos, "Optical imaging of cancer heterogeneity with multispectral optoacoustic tomography," Radiology **263**(2), 461–468 (2012).
10. C. L. Didychuk, P. Ephrat, A. Chamson-Reig, S. L. Jacques, and J. J. L. Carson, "Depth of photothermal conversion of gold nanorods embedded in a tissue-like phantom," Nanotechnology **20**(19), 195102 (2009).
11. L.-C. Chen, C.-W. Wei, J. S. Souris, S.-H. Cheng, C.-T. Chen, C.-S. Yang, P.-C. Li, and L.-W. Lo, "Enhanced photoacoustic stability of gold nanorods by silica matrix confinement," J. Biomed. Opt. **15**(1), 016010 (2010).
12. Y.-S. Chen, W. Frey, S. Kim, K. Homan, P. Kruizinga, K. Sokolov, and S. Emelianov, "Enhanced thermal stability of silica-coated gold nanorods for photoacoustic imaging and image-guided therapy," Opt. Express **18**(9), 8867–8878 (2010).
13. L. Cavigli, M. de Angelis, F. Ratto, P. Matteini, F. Rossi, S. Centi, F. Fusi, and R. Pini, "Size Affects the Stability of the Photoacoustic Conversion of Gold Nanorods," J. Phys. Chem. C **118**(29), 16140–16146 (2014).
14. A. M. Fales, W. C. Vogt, T. J. Pfefer, and I. K. Ilev, "Quantitative Evaluation of Nanosecond Pulsed Laser-Induced Photomodification of Plasmonic Gold Nanoparticles," Sci. Rep. **7**(1), 15704 (2017).
15. S. L. Jacques, "Optical properties of biological tissues: a review," Phys. Med. Biol. **58**(11), R37–R61 (2013).
16. W. C. Vogt, C. Jia, K. A. Wear, B. S. Garra, and T. Joshua Pfefer, "Biologically relevant photoacoustic imaging phantoms with tunable optical and acoustic properties," J. Biomed. Opt. **21**(10), 101405 (2016).
17. B. T. Cox, J. G. Laufer, P. C. Beard and S. R. Arridge, "Quantitative spectroscopic photoacoustic imaging: a review," J. Biomed. Opt. **17**, 061202 (2012).
18. L. Wang, S. L. Jacques, and L. Zheng, "MCML--Monte Carlo modeling of light transport in multi-layered tissues," Comput. Methods Programs Biomed. **47**(2), 131–146 (1995).
19. H. J. van Staveren, C. J. M. Moes, J. van Marie, S. A. Prahl, and M. J. C. van Gemert, "Light scattering in Intralipid-10% in the wavelength range of 400-1100 nm," Appl. Opt. **30**(31), 4507–4514 (1991).
20. S. Walt, S. C. Colbert, and G. Varoquaux, "The NumPy Array: A Structure for Efficient Numerical Computation," Comput. Sci. Eng. **13**(2), 22–30 (2011).
21. J. D. Hunter, "Matplotlib: A 2D Graphics Environment," Comput. Sci. Eng. **9**(3), 90–95 (2007).
[22] E. Jones, T. Oliphant, and P. Peterson and others, [SciPy: Open Source Scientific Tools for Python], (2001 -).
23. T. Gould, Q. Wang, and T. J. Pfefer, "Optical-thermal light-tissue interactions during photoacoustic breast imaging," Biomed. Opt. Express **5**(3), 832–847 (2014).
24. S.-S. Chang, C.-W. Shih, C.-D. Chen, W.-C. Lai, and C. R. C. Wang, "The Shape Transition of Gold Nanorods," Langmuir **15**(3), 701–709 (1999).
25. S. Link, C. Burda, B. Nikoobakht, and M. A. El-Sayed, "Laser-Induced Shape Changes of Colloidal Gold Nanorods Using Femtosecond and Nanosecond Laser Pulses," J. Phys. Chem. B **104**(26), 6152–6163 (2000).

Biomedical Optics EXPRESS

26. S. Link, Z. L. Wang, and M. A. El-Sayed, "How Does a Gold Nanorod Melt?" J. Phys. Chem. B **104**(33), 7867–7870 (2000).
27. C. J. DeSantis, D. Huang, H. Zhang, N. J. Hogan, H. Zhao, Y. Zhang, A. Manjavacas, Y. Zhang, W.-S. Chang, P. Nordlander, S. Link, and N. J. Halas, "Laser-Induced Spectral Hole-Burning through a Broadband Distribution of Au Nanorods," J. Phys. Chem. C **120**(37), 20518–20524 (2016).
28. Y. Horiguchi, K. Honda, Y. Kato, N. Nakashima, and Y. Niidome, "Photothermal reshaping of gold nanorods depends on the passivating layers of the nanorod surfaces," Langmuir **24**(20), 12026–12031 (2008).
29. P. Li, Y. Wu, D. Li, X. Su, C. Luo, Y. Wang, J. Hu, G. Li, H. Jiang, and W. Zhang, "Seed-Mediated Synthesis of Tunable-Aspect-Ratio Gold Nanorods for Near-Infrared Photoacoustic Imaging," Nanoscale Res. Lett. **13**(1), 313 (2018).
30. H. Kang, S.-W. Lee, S.-M. Park, S.-W. Cho, J. Y. Lee, C.-S. Kim, and T. G. Lee, "Real-time functional optical-resolution photoacoustic microscopy using high-speed alternating illumination at 532 and 1064 nm," J. Biophotonics **11**(3), e201700210 (2018).
31. M. Lakshman and A. Needles, "Screening and quantification of the tumor microenvironment with micro-ultrasound and photoacoustic imaging," Nat. Methods **12**(4), 372 (2015).
32. D. A. Nedosekin, T. Fahmi, Z. A. Nima, J. Nolan, C. Cai, M. Sarimollaoglu, E. Dervishi, A. Basnakian, A. S. Biris, and V. P. Zharov, "Photoacoustic *in vitro* flow cytometry for nanomaterial research," Photoacoustics **6**, 16–25 (2017).
33. E. C. Cho, J. Xie, P. A. Wurm, and Y. Xia, "Understanding the role of surface charges in cellular adsorption versus internalization by selectively removing gold nanoparticles on the cell surface with a I2/KI etchant," Nano Lett. **9**(3), 1080–1084 (2009).
34. M. J. Crow, K. Seekell, J. H. Ostrander, and A. Wax, "Monitoring of receptor dimerization using plasmonic coupling of gold nanoparticles," ACS Nano **5**(11), 8532–8540 (2011).
35. J. Zhong, L. Wen, S. Yang, L. Xiang, Q. Chen, and D. Xing, "Imaging-guided high-efficient photoacoustic tumor therapy with targeting gold nanorods," Nanomedicine (Lond.) **11**(6), 1499–1509 (2015).
36. J. Park, A. Estrada, J. A. Schwartz, P. Diagaradjane, S. Krishnan, A. K. Dunn, and J. W. Tunnell, "Intra-organ biodistribution of gold nanoparticles using intrinsic two-photon-induced photoluminescence," Lasers Surg. Med. **42**(7), 630–639 (2010).
37. G. B. Braun, T. Friman, H.-B. Pang, A. Pallaoro, T. Hurtado de Mendoza, A.-M. A. Willmore, V. R. Kotamraju, A. P. Mann, Z.-G. She, K. N. Sugahara, N. O. Reich, T. Teesalu, and E. Ruoslahti, "Etchable plasmonic nanoparticle probes to image and quantify cellular internalization," Nat. Mater. **13**(9), 904–911 (2014).
38. R. Xiong, S. K. Samal, J. Demeester, *et al*., "Laser-assisted photoporation: fundamentals, technological advances and applications," Advances in Physics: X **1**(4), 596–620 (2016).
39. E. Y. Lukianova-Hleb, Y.-S. Kim, I. Belatsarkouski, A. M. Gillenwater, B. E. O'Neill, and D. O. Lapotko, "Intraoperative diagnostics and elimination of residual microtumours with plasmonic nanobubbles," Nat. Nanotechnol. **11**(6), 525–532 (2016).
40. A. M. Wilson, J. Mazzaferri, É. Bergeron, S. Patskovsky, P. Marcoux-Valiquette, S. Costantino, P. Sapieha, and M. Meunier, "In Vivo Laser-Mediated Retinal Ganglion Cell Optoporation Using $K_V1.1$ Conjugated Gold Nanoparticles," Nano Lett. **18**(11), 6981–6988 (2018).
41. L. Gentemann, S. Kalies, M. Coffee, H. Meyer, T. Ripken, A. Heisterkamp, R. Zweigerdt, and D. Heinemann, "Modulation of cardiomyocyte activity using pulsed laser irradiated gold nanoparticles," Biomed. Opt. Express **8**(1), 177–192 (2016).
42. C. Paviolo and P. R. Stoddart, "Gold Nanoparticles for Modulating Neuronal Behavior," Nanomaterials (Basel) **7**(4), 92 (2017).
43. Y. Wang and L. Guo, "Nanomaterial-Enabled Neural Stimulation," Front. Neurosci. **10**(69), 69 (2016).